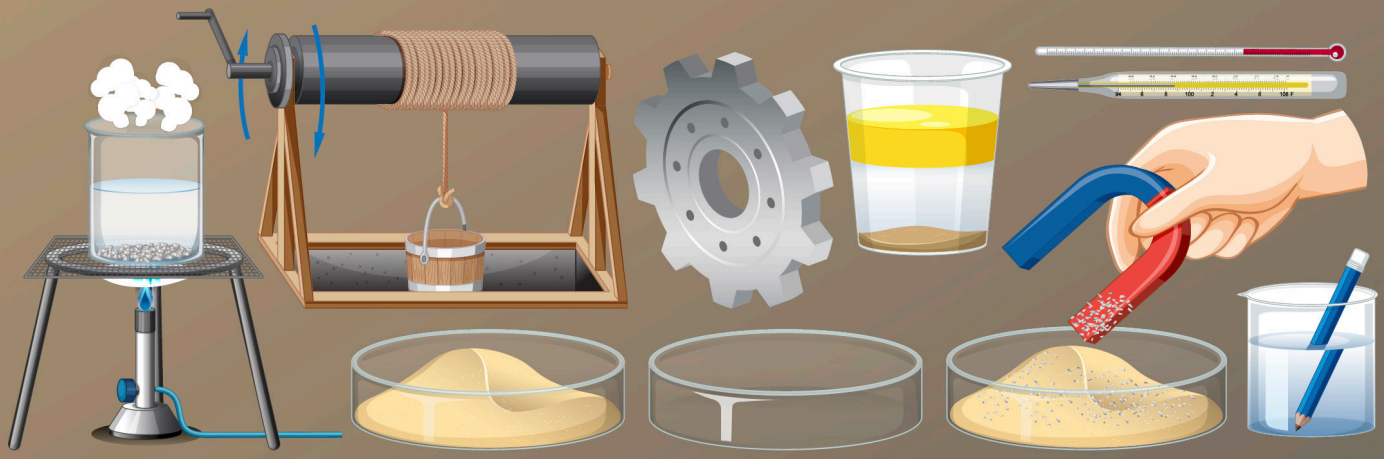
# American Journal of Advanced Materials Research (AJAMR)

ISSN: 3070-2011 (ONLINE)

VOLUME 2 ISSUE 1 (2026)



PUBLISHED BY
E-PALLI PUBLISHERS, DELAWARE, USA

American Journal of
Advanced Materials Research (AJAMR)

Volume 2 Issue 1, Year 2026
ISSN: 3070-2011 (Online)
DOI: https://doi.org/10.54536/ajamr.v2i1.8945
https://journals.e-palli.com/home/index.php/ajamr

# A Circular Economy Approach to Wastewater Treatment: Utilizing Fish Scale and Rice Husk Ash Composites for Methylene Blue Removal

Daniel W Kisauli[1*], Francis Maingi[1], Linda Ouma[1]

**Article Information**

**Received:** August 20, 2026

**Accepted:** November 02, 2026

**Published:** November 27, 2026

**Keywords**

*Adsorption, Composite, Fish Scales, Methylene Blue, Wastewater*

## ABSTRACT

Dye effluents heavily pollute water bodies, presenting severe threats to public health and ecosystems. To address this, a novel chitosan–silica composite was synthesized using waste fish scales and rice husk ash, then evaluated for its efficiency in removing methylene blue (MB) dye from wastewater. The process successfully cross-linked the chitosan and sodium silicate, as confirmed by XRD, Raman, XRF, and FT-IR spectroscopy. Integrating the inorganic silica support enhanced the composite's mechanical stability and introduced additional binding sites compared to pure chitosan. Batch adsorption studies optimized the removal conditions at a pH of 10, 0.4 g adsorbent dosage, 120-minute contact time, and 50 mg/L initial dye concentration. The equilibrium data adhered closely to the Langmuir isotherm model (R2 = 0.939), yielding a maximum monolayer adsorption capacity (Qmax) of 9.217 mg/g and a Langmuir constant ((KL) of 0.154 L/mg. These results demonstrate that MB adsorption occurs as a monolayer on homogeneous, deprotonated silanol sites. Ultimately, this study highlights the viability of recycling fish scales and rice husk ash into effective, sustainable adsorbents for industrial wastewater treatment

## INTRODUCTION

Textile and leather industrial operations discharge synthetic dye effluents into natural water bodies. These persistent pollutants resist biological and photocatalytic degradation, making them exceptionally difficult to remediate (Soltani, 2021; Elzahar *et al.*, 2023). Even at low concentrations, they inhibit photosynthesis, disrupt aquatic food chains, and exert toxic effects on aquatic life (Kyomuhimbo *et al.*, 2024). Methylene blue, a common cationic dye, represents a typical pollutant found in these industrial waste streams (Gupta, 2021). While conventional wastewater treatment methods such as coagulation/flocculation, chemical oxidation, ozonation, and membrane filtration are widely used, they present distinct drawbacks. Specifically, membrane filtration suffers from membrane fouling (Gisi *et al.*, 2020), and high maintenance costs; biological processes struggle to degrade recalcitrant synthetic structures; and chemical oxidation and ozonation often produce toxic secondary by-products (Kyomuhimbo *et al.*, 2024). Furthermore, the efficiency of these conventional systems drops significantly at lower dye concentrations (Mishra *et al.*, 2021; Elhady *et al.*, 2024).

Consequently, adsorption has emerged as a highly promising alternative due to its operational simplicity, cost-effectiveness, versatility, and capability to achieve high removal efficiencies without producing hazardous secondary waste (Soltani, 2021; Elhady *et al.*, 2024). Although activated carbon is traditionally preferred, its widespread commercial application is hindered by high production costs and complex regeneration processes (Ngulube *et al.*, 2020; Elzahar *et al.*, 2023; Elhady *et al.*, 2024). This limitation has driven research toward sustainable, low-cost, bio-based alternatives. Among these, chitosan a linear biopolymer produced by deacetylating chitin found abundantly in crustacean shells and fish scales shows great potential. Its abundant amino ($–NH_2$) and hydroxyl (–OH) functional groups readily facilitate dye removal through electrostatic attraction, hydrogen bonding, and surface complexation (Kaya *et al.*, 2022; Elzahar *et al.*, 2023; Wang *et al.*, 2023).

Despite its potential, chitosan is limited by poor mechanical strength and high solubility in acidic environments, which hinders its application in industrial dye remediation (Crini & Badot, 2020; Abdulrahman *et al.*, 2021). To address these drawbacks, researchers have focused on hybridizing chitosan with inorganic supports like silica ($SiO_2$) (Kyomuhimbo *et al.*, 2024; Li *et al.*, 2024). The silica framework introduces a rigid inorganic matrix that enhances mechanical stability, thermal resistance, and porous architecture. Consequently, chitosan–silica composites exhibit superior adsorption capacities, better reusability, and greater structural integrity than neat chitosan (Blachnio *et al.*, 2023; Elhady *et al.*, 2024). For cationic contaminants like methylene blue, adsorption is primarily driven by the silica component; when the solution pH exceeds the point of zero charge, silanol (Si–OH) groups are deprotonate into negatively charged $Si–O^-$, which electrostatically attracts the cationic dye molecules (Lan *et al.*, 2022; Zhong *et al.*, 2023). Utilizing rice husk ash as an economical silica precursor allows for the extraction of soluble sodium silicate via alkaline treatment (Sapei *et al.*, 2021; Bakar *et al.*, 2022). Integrating this bio-derived silica into a chitosan matrix via sol-gel

[1] Department of Science Technology and Engineering, Kibabii University, Bungoma, Kenya
[*] Corresponding author's e-mail: kisaulidaniel@gmail.com

encapsulation preserves the active dye-binding sites of chitosan while reinforcing the composite's structural strength. Accordingly, this study details the synthesis and characterization of a novel chitosan–silica composite fabricated from tilapia fish scales and rice husk ash wastes, evaluating its performance for methylene blue removal from aqueous solutions.

## MATERIALS AND METHODS

### Chemicals and Reagents

Tilapia fish scales were used as a source of chitosan, while the rice husk ash was used as a source of silica. The fish scales were waste materials obtained from Dunga beach in Kisumu. NaOH was used to prepare sodium silicate and in pH adjustment during batch studies. HCl was used for demineralization and in the pH adjustment of batch studies. The pH of the gelling mixture was adjusted using acetic acid. 50% ethanol was used to wash the gel to minimize shrinkage during drying. Methylene blue was used to prepare synthetic wastewater. All these reagents were of analytical grade and used without further purification.

### Extraction of chitosan from fish scale waste

The isolation of chitosan involved five primary stages: pretreatment, demineralization, deproteinization, deacetylation, and purification (Rinaudo, 2020; Younes *et al.*, 2020). First, raw fish scales were thoroughly rinsed under running tap water to eliminate impurities, followed by drying in a hot-air oven at 60°C for 24 hours. To remove calcium carbonate and mineral deposits, the dried scales were agitated in 1 M HCl for 6 hours at room temperature (26°C), and subsequently rinsed with distilled water until a neutral pH was reached. Protein removal was achieved by treating the demineralized scales with 1 M NaOH at 75°C for 2 hours under continuous stirring to yield chitin; the sample was then washed back to neutrality. Deacetylation of the chitin into chitosan was carried out using 1.25 M NaOH at 80°C for 2 hours with constant heating and stirring, achieving a degree of deacetylation greater than 70% (Kaya *et al.*, 2022). Finally, the purified chitosan was washed to a neutral pH with distilled water, dried in an oven at 60°C for 3 hours, and pulverized into a fine white powder/ Figure 1 shows chitosan powder obtained after deacetylation and drying.



**Figure 1**: Chitosan powder obtained after deacetylation and drying.

### Extraction of silica from rice husk ash

To prepare the silica precursor, we calcined rice husks in a kiln at 600°C for 4 hours, (Jonathan, 2020; Chun & Lee, 2020). After turning off the kiln, the material cooled inside for approximately 1 hour. This process yielded 45 g of white rice husk ash (shown in Figure 2), which we weighed and utilized to synthesize sodium silicate.



**Figure 2**: Rice husk ash obtained after calcination at 600°C.

### Preparation of sodium silicate

30 g of rice husk ash was combined with 240 mL of a 2 M NaOH solution (Ermania Em Wogo *et al.*, 2022). The mixture underwent heating at 75°C for 2 hours under continuous stirring. Once cooled to room temperature, the solution was filtered to separate the clear sodium silicate filtrate from the remaining black, carbon-rich residue. The corresponding chemical reaction is illustrated in Equation 1 (Sapei *et al.*, 2021; Bakar *et al.*, 2022).

$$SiO_2(s) + 2NaOH\ (aq) \rightarrow Na_2SiO_3\ (aq) + H_2O\ (l) \ldots\ldots 1$$

The chitosan solution was synthesized by dissolving 20 g of chitosan powder in 1 L of 2% acetic acid (1 g: 50 mL ratio) under continuous room-temperature stirring for 2 h (Rinaudo *et al.*, 1999). Subsequently, 240 mL of sodium silicate was introduced into the solution. This mixture was stirred vigorously for 2 h to induce chitosan–silica gel formation. The resulting gel was then titrated with 5% acetic acid until a pH of 4.5 was achieved, following the general reaction mechanism shown in Equation 2 (Blachnio *et al.*, 2023; Bratskaya *et al.*, 2022).

$$\text{Chitosan} + Na_2SiO_3 + H^+ \rightarrow \text{Chitosan–}SiO_2\ \text{(composite)} + Na^+ + H_2O(l) \ldots\ldots\ldots 2$$

To allow for aging, the chitosan–silica gel was kept at room temperature for 1 hour. This process promotes the condensation of silanol groups (Si–OH) into siloxane (Si–O–Si) linkages, forming the 3-D composite skeletal structure illustrated in Equation 3 (Blachnio *et al.*, 2023).

$$Si\text{–}OH\ (aq) + HO\text{–}Si(aq) \rightarrow Si\text{–}O\text{–}Si(aq) + H_2O(l) \ldots\ldots 3$$

Thereafter, the gel was washed with distilled water to neutral pH. A final wash with 50% ethanol was done on the gel to minimize shrinkage during drying. The gel was oven-dried at 60°C for 12 hours to obtain a white solid, which was ground with a mortar and pestle to obtain the chitosan–silica composite powder.

**Batch Adsorption Studies**

Methylene blue adsorption was conducted using a batch method adapted from Blachnio *et al.* (2023). First, a 1,000 mg/L stock solution was prepared by dissolving 1 g of methylene blue dye in distilled water within a volumetric flask, filling it to the calibration mark. This stock solution was stored in a dark bottle to inhibit photochemical degradation. Experimental working solutions were then prepared via serial dilution ($C_1V_1 = C_2V_2$). For each batch run, a known mass of the composite was introduced to 50 mL of dye solution in a 100 mL beaker and agitated on a mechanical shaker at 150 rpm. Following the predetermined contact time, the mixture was filtered. The residual dye concentration in the filtrate was quantified using a UV-Vis spectrophotometer at blue (λ max = 664 nm). Finally, the percentage removal (%R) and equilibrium adsorption capacity ($q_e$) were evaluated using Equations 4 and 5.

where $C_o$ and $C_e$ (mg/L) are the initial and equilibrium

$$\%R = [(C_o - C_e) / C_o] \times 100 \ldots\ldots\ldots 4$$

$$q_e = (C_o - C_e)\ V / m \ldots\ldots\ldots 5$$

methylene blue concentrations, m (g) is the adsorbent mass, and V (L) is the solution volume. Graphs of removal efficiency against the investigated parameters were plotted to see the relationship.

**Effect of Solution pH**

The effect of pH on methylene blue adsorption was evaluated from pH 2 to 14. Solutions (50 mL, 50 mg/L) at each specified pH adjusted with 0.1 M NaOH/HCl and verified via a digital pH meter were shaken with 0.1 g of the composite at 150 rpm and 25°C for 120 minutes. Residual dye concentrations were measured using UV-Vis's spectrophotometer.

**Effect of Adsorbent Dosage**

To evaluate the effect of dosage, varying amounts of the chitosan–silica composite (0.1 to 0.5 g) were added to separate 100 mL beakers containing 50 mL of a 50 mg/L methylene blue solution. The mixtures were agitated at 150 rpm and 25°C for an equilibrium time of 120 minutes. Filtration was done and the remaining dye concentrations were determined using a UV-Vis spectrophotometer.

**Effect of Contact Time**

To evaluate the effect of contact time, the agitation period was varied from 20 to 140 min using 0.1 g of the composite in a 50 mL methylene blue solution (50 mg/L) at pH 8, 150 rpm, and room temperature. At each specified time interval, a beaker was removed from the shaker, and the solution was filtered. The residual dye concentration in the filtrate was then determined via UV-Vis spectrophotometry. The equilibrium contact time was established as the point where no significant decrease in dye absorbance was observed.

**Effect of Initial Dye Concentration**

To evaluate how initial dye concentration affects adsorption, the stock solution was diluted to prepare working concentrations ranging from 40 to 120 mg/L (40, 50, 60, 80, 100, and 120 mg/L). For each experiment, 0.1 g of the composite was added to 50 mL of the respective dye solution. The mixtures were agitated at 150 rpm on a mechanical shaker at a constant temperature of 25°C for 120 minutes. Following filtration, the residual dye concentrations were quantified using UV-Vis spectroscopy.

**Adsorption Isotherms**

To evaluate equilibrium isotherms, 0.1 g of the chitosan–silica composite was mixed with 50 mL of methylene blue solutions at initial concentrations ranging from 40 to 120 mg/L. After shaking the mixtures for 120 minutes at 25°C, researchers fitted the resulting equilibrium data to the linear forms of the Freundlich and Langmuir isotherm models (Equations 6 and 7), respectively (Blachnio *et al.*, 2023).

$$\log q_e = (1/n) \log C_e + \log K^f \ldots\ldots\ldots\ldots 6$$

$$C_e/q_e = C_e/Q_m + 1/(K_L Q_m) \ldots\ldots\ldots 7$$

Where $q_e$ (mg/g) is the equilibrium adsorption capacity, (mg/L) is the equilibrium concentration, $Q_m$ (mg/g) is the maximum Langmuir monolayer adsorption capacity, $K_L$ (L/mg) is the Langmuir equilibrium constant, $K^f$ (mg/g) is the Freundlich adsorption capacity constant, and (1/n) is the heterogeneity factor. Model goodness-of-fit was evaluated using the coefficient of determination ($R^2$).

## RESULTS AND DISCUSSION

### X-Ray Fluorescence (XRF) Analysis

Table 1 shows the elemental/oxide composition of chitosan as obtained using XRF

**Table 1**: Elemental/oxide composition of chitosan using XRF

| Element/Oxide | Mean % | SD (±) |
|---|---|---|
| MgO | 18.563 | 2.469 |
| $Al_2O_3$ | 2.491 | 0.371 |
| $P_2O_5$ | 28.573 | 0.287 |
| S | 1.618 | 0.062 |
| Cl | 0.164 | 0.029 |
| CaO | 46.881 | 0.143 |
| $TiO_2$ | 0.050 | 0.013 |
| MnO | 0.016 | 0.009 |
| $Fe_2O_3$ | 1.239 | 0.037 |
| Cu | 0.125 | 0.007 |
| As | 0.065 | 0.004 |
| Sr | 0.178 | 0.004 |

The main chemical components of the extracted chitosan were phosphorus pentoxide (28.573%) and calcium oxide (46.881%), which correspond to the residual hydroxyapatite and calcium carbonate retained from the fish scales after deproteinization and deacetylation, since chitosan extraction does not fully remove the inorganic calcium phosphate matrix. Magnesium oxide (18.563%) and aluminium oxide (2.491%) were minor mineral components, while sulphur and iron oxide were trace inorganic residues from the processing solutions. At this point, no silica was found, indicating that no silica source had been added to the chitosan. Table 2 shows the elemental composition of the chitosan-silica composite.

**Table 2**: Elemental/oxide composition of the chitosan–silica composite by XRF

| Element/Oxide | Mean % | SD (±) |
|---|---|---|
| $SiO_2$ | 60.916 | 0.313 |
| $P_2O_5$ | 2.764 | 0.063 |
| S | 14.868 | 0.066 |
| Cl | 0.876 | 0.027 |
| CaO | 14.136 | 0.034 |
| $TiO_2$ | 0.280 | 0.012 |
| MnO | 0.016 | 0.007 |
| $Fe_2O_3$ | 4.921 | 0.028 |
| Cu | 0.736 | 0.007 |
| As | 0.343 | 0.005 |
| Sr | 0.141 | 0.004 |

XRF analysis confirmed that silica is the dominant constituent (91.862%) of the calcined rice husk ash, validating its role as a low-cost, high-purity precursor. In the resulting chitosan–silica composite, silicon dioxide remains the primary component at 60.916%, proving that the silica introduced during the sol-gel process was successfully retained. While calcium oxide (14.136%) and sulphur (14.868%) remained prominent, phosphorus pentoxide decreased to roughly 3% due to the dilution of the chitosan matrix by the added sodium silicate. Conversely, iron oxide, copper, and arsenic absent in the raw chitosan emerged as trace impurities introduced by the silica precursor during encapsulation. Meanwhile, magnesium and aluminium oxides fell below detection

limits due to dilution during cross-linking (Xu *et al.*, 2021). Ultimately, the high concentration of silica in the XRF data provides clear evidence of its successful incorporation into the chitosan matrix.

**X-ray Diffraction (XRD) Analysis**

The crystallographic structure and degree of crystallinity of synthesized chitosan and the chitosan–silica composite was investigated using XRD (D6 PHASER serial number 5117) to assess whether the crystallographic properties of chitosan were influenced by the formation of the composite (Blachnio *et al.*, 2023). The figure below shows the X-ray diffractogram of the synthesized chitosan sample. X-ray diffraction (XRD) analysis was performed to evaluate the crystallographic structure and degree of crystallinity of both the synthesized chitosan and the chitosan–silica composite. This characterization aimed to determine if the structural properties of the chitosan matrix were altered upon composite formation (Blachnio *et al.*, 2023). The resulting X-ray diffractogram for the synthesized chitosan sample is displayed in Figure 3

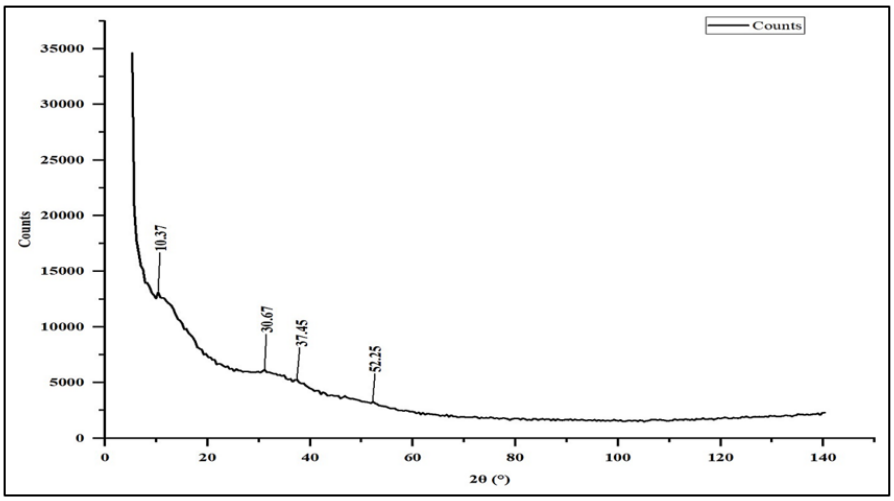



**Figure 3**: X-ray diffractogram of the synthesized chitosan sample (Using XRD D6 PHASER serial number 5117).

The XRD pattern of chitosan (Figure 3) was characterized by a broad, high-intensity background featuring a single prom-inent inflection at 2θ = 10.37°. This peak corresponds to the semicrystalline hydrated allomorph of chitosan, which arises from partially ordered glucosamine chains stabilized by intermolecular hydrogen bonding between free amine and hy-droxyl groups (Khabibullaeva *et al.*, 2022). The undisturbed nature of this peak confirms the absence of a silica phase that could disrupt the hydrogen-bonded packing of the native polymer. Additionally, three weak, poorly resolved reflec-tions emerge from the sloping background at 30.67°, 37.45°, and 52.25°. The reflection at 30.67° falls between the stand-ard values for calcite (29.41°, ICDD 00-005-0586) and halite (31.71°, ICDD 00-005-0628), suggesting an overlapping signal. The peak at 37.45° aligns closely with low quartz (110) at 36.54° (ICDD 00-046-1045). These minor reflections represent trace calcite, halite, and quartz residues introduced during the demineralization and neutralization of the fish-scale matrix (Ade *et al.*, 2020). Meanwhile, the peak at 52.25° cannot be definitively matched to these phases and is clas-sified as a low-intensity residual reflection. Collectively, these features establish the crystallographic baseline of a semi-crystalline chitosan matrix containing only trace inorganic impurities and no silica component prior to composite fabrica-tion. The XRD pattern of the resulting chitosan-silica composite is presented in Figure 4.

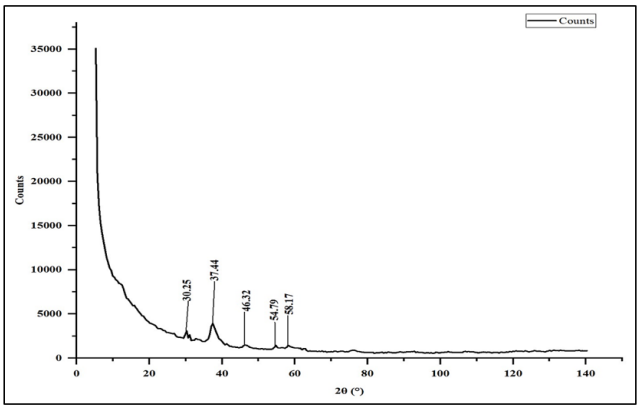



**Figure 4**: X-ray diffractogram of the chitosan–silica composite

The primary distinction between the composite (Figure 4) and unmodified chitosan diffractograms is the complete disappearance of the 2θ = 10.37° reflection. This absence stems from the sol-gel process, where the hydrolysis and polycondensation of the silica precursor generate silanol (Si–OH) groups. These groups condense with the specific amine and hydroxyl functionalities that normally drive chitosan's self-hydrogen bonding. Occupying these sites via silica anchoring deprives the glucosamine chains of the structural cohesion required to maintain the resolvable (020) reflection (Khabibullaeva *et al.*, 2022). Consequently, the composite profile exhibits a broad, diffuse halo characteristic of an amorphous silica phase, alongside reduced peak intensities and line broadening relative to neat chitosan. This confirms that the silica network disrupts the long-range order of the polymer chains. Meanwhile, weak residual reflections persist at 2θ values of 30.25°, 37.44°, 46.32°, 54.79° and 58.17°. The first two align with the calcite/halite overlap and the low-quartz (110) reflections present in the unmodified polymer. The peaks at 46.32°, 54.79° and 54.87° correspond to halite (220), low-quartz (202), and calcite (1 0 10), matching ICDD references 00-005-0628 45.46°, 00-046-1045 54.87°, and 00-005-0586 58.08°, respectively. Because all five signals belong to the native calcite–halite–quartz residue assembly, no new crystalline silica phases were formed. Instead, the silica exists as an amorphous network embedded within the chitosan matrix, consistent with literature on analogous hybrid systems (Blachnio *et al.*, 2023). Notably, the 37.44° peak appears most prominent in the composite pattern; the suppression of the semicrystalline chitosan halo by the silica network minimizes background scattering, thereby enhancing the resolution of these underlying mineral reflections

**Raman Spectroscopic Analysis**

Raman spectroscopy was employed to investigate the molecular bonding environments of both pristine chitosan and the composite. While X-ray diffraction (XRD) primarily captures long-range crystalline order, Raman scattering detects local vibrational modes. This makes it ideal for identifying the amine, hydroxyl, and glycosidic linkages that drive chitosan's dye-binding capacity, as well as any novel bonds resulting from silica integration. Figure 5 illustrates the Raman spec-trum of the fish-scale-extracted chitosan.

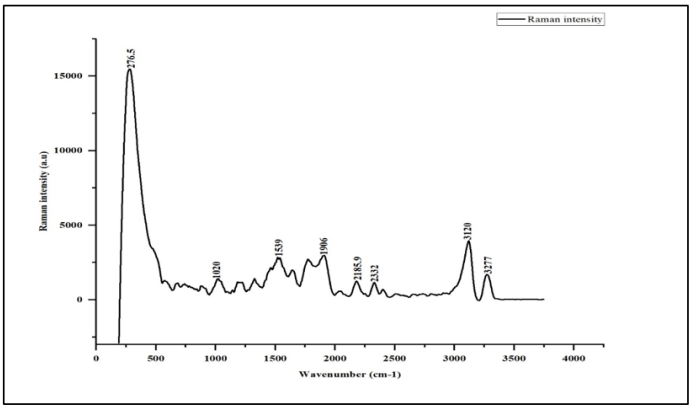



**Figure 5**: Raman spectrum of chitosan extracted from fish scales.

The Raman spectrum of pristine chitosan (Figure 5) exhibits a low-wavenumber band at 276.5 $cm^{-1}$, which corresponds to the lattice vibrations of the polysaccharide backbone. Additionally, the prominent bands observed at 1020 $cm^{-1}$ and 1539 $cm^{-1}$ are assigned to C–O/C–O–C glycosidic stretching and N–H bending/C–N stretching vibrations, respectively. These peaks are highly characteristic of the amine and amide functional groups typically found in deacetylated chitin (Kačuráková *et al.*, 2020; Zhou *et al.*, 2022). A minor band at 1906 $cm^{-1}$ represents an overtone vibration, while the broad envelope spanning 3000 to 3300 $cm^{-1}$ resolves into distinct peaks at 3120 $cm^{-1}$ and 3277 $cm^{-1}$. These are attributed to the O–H and N–H stretching vibrations of the hydroxyl and amine groups, which play a pivotal role in chitosan's dye-binding mechanism. Collectively, the appearance of these distinct fingerprint bands confirms that the extraction protocol successfully maintained the fundamental chemical integrity of the biopolymer. To evaluate structural modifications, Figure 6 illustrates the Raman spectrum of the chitosan-silica composite derived from fish scales and rice husk ash. This spectrum was acquired under identical experimental conditions, ensuring that any subsequent peak shifts or band splitting can be confidently ascribed to the structural incorporation of silica into the chitosan matrix, rather than instrumental or environmental variance.

Sol-gel encapsulation with rice-husk-ash-derived silica induced several distinct spectral shifts in the composite material (Figure 6). The low-frequency band migrated from 276.5 $cm^{-1}$ to 296.2 $cm^{-1}$, signalling the development of a novel chitosan–silica vibrational network. Additionally, the C–O stretching region overlapped with the symmetric and asymmetric Si–O–Si stretching modes of the silica matrix. The appearance of a highly resolved band at 1646 $cm^{-1}$ (amide I, C=O stretching), alongside the preserved 1324 $cm^{-1}$ band, points to reorganized carbonyl and amide environments driven by hydrogen bonding

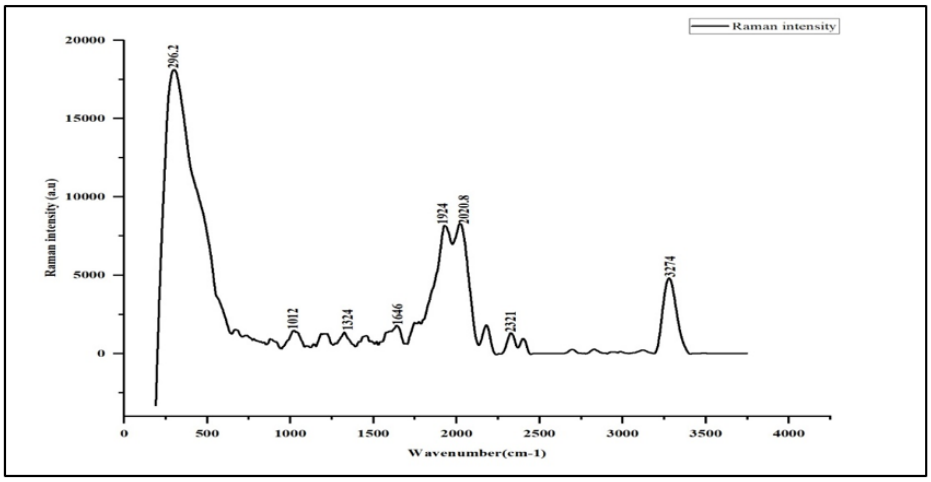



**Figure 6**: Raman spectrum of the chitosan–silica composite.

between the amine/hydroxyl groups of chitosan and the silanol groups of silica. Notably, between 1900 and 2100 $cm^{-1}$, the solitary 1906 $cm^{-1}$ chitosan band intensified and resolved into a doublet at 1924 $cm^{-1}$ and 2020.8 $cm^{-1}$, confirming a highly ordered interfacial hydrogen-bonding network (Al Sagheer & Muslim, 2009). Ultimately, these structural modifications align with an enhanced mechanical profile, increased binding site accessibility, and an expanded effective surface area for adsorption compared to pristine chitosan (Maingi *et al.*, 2022).

**FT-IR Characterization**

Fourier-transform infrared (FT-IR) spectroscopy confirmed the successful hybridization of the phases by identifying the functional groups in both chitosan and the chitosan–silica composite. Because FT-IR is highly sensitive to the amine, hydroxyl, and silanol groups responsible for dye binding, it directly complements the structural data gathered from XRD and Raman spectroscopy. The specific FT-IR spectrum for fish-scale-derived chitosan is illustrated in the spectrum below (Figure 7).

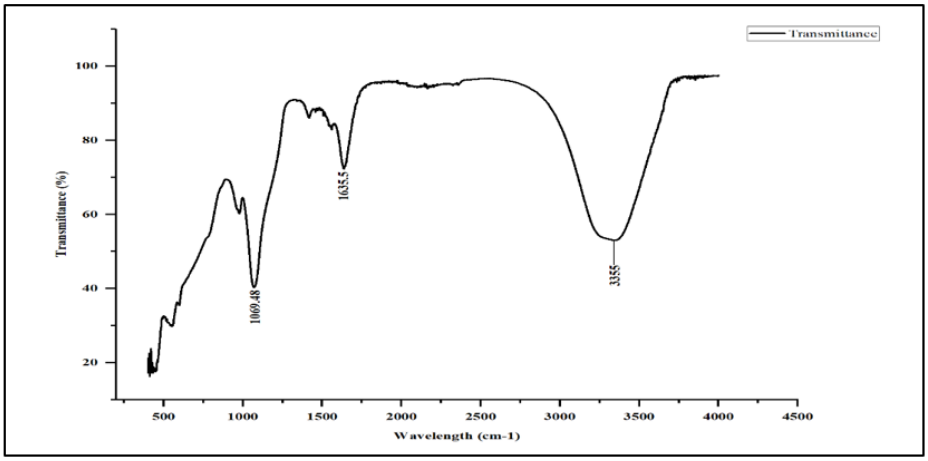



**Figure 7**: FT-IR spectrum of chitosan extracted from fish scales.

The FT-IR profile of chitosan (Figure 7) reveals a broad absorption band centered at 3450 $cm^{-1}$, signalling the overlapping stretching vibrations of N–H and O–H groups involved in robust inter- and intramolecular hydrogen bonding network networks (Brugnerotto *et al.*, 2001; Kasaai, 2008). Ambient background conditions introduce a minor artifact near 2360 $cm^{-1}$ corresponding to atmospheric $CO_2$, which does not reflect the intrinsic polymer chemistry (Stuart, 2004). Key structural benchmarks include the Amide I and Amide II bands (1650–1550 $cm^{-1}$), which serve as markers for the degree of deacetylation calculated here to be greater than 70% (Brugnerotto *et al.*, 2001; Kasaai, 2008). Successful preservation of the core polysaccharide architecture is validated by distinct peaks at 1420 $cm^{-1}$ (C–H bending and C–N stretching) and a collection of bands between 1000 and 1150 $cm^{-1}$ (C–O and C–O–C glycosidic stretching). Additionally, the low-intensity bands within the 900–800 $cm^{-1}$ region match the typical vibrations of the glucopyranose ring and β-(1→4)-glycosidic linkages, while a prominent peak at 470 $cm^{-1}$ represents skeletal deformation modes that confirm structural integrity (Stuart, 2004). The subsequent spectrum illustrates the chitosan-silica composite, captured using identical experimental parameters to facilitate a direct, line-by-line comparison with the unmodified chitosan baseline

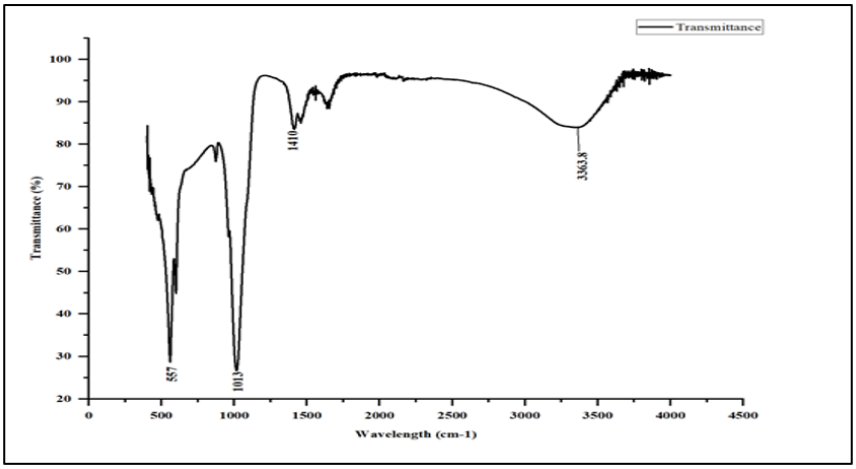



**Figure 8**: FT-IR spectrum of the chitosan–silica composite.

Figure 8 illustrates the composite spectrum, which retains the characteristic chitosan profile but is dominated by the vibrational modes of the silica network. The attenuation and narrowing of the N–H/O–H band near 3450 $cm^{-1}$ indicate a reduced density of free amine and hydroxyl groups, stemming from their hydrogen-bonding interactions with surface silanol (Si–OH) groups. Concurrently, the preservation of the Amide I and Amide II bands near 1650 and 1550 $cm^{-1}$ confirms the integrity of the underlying chitosan framework.

The most pronounced spectral alteration occurs within the C–O–C region. While pristine chitosan exhibits a moderate band near 1030 $cm^{-1}$, the composite displays a strong, broad absorption band spanning 1000–1150 $cm^{-1}$ with a distinct minimum near 1080 $cm^{-1}$. This feature is assigned to the asymmetric Si–O–Si stretching vibrations of the silica network synthesized from rice husk ash (Saiful, 2022). Furthermore, the shoulder observed at 950–960 $cm^{-1}$ corresponds to Si–OH stretching, whereas the recovered transmittance near 800 $cm^{-1}$ is attributed to symmetric Si–O–Si stretching superimposed onto the skeletal vibrations of chitosan (Saiful, 2022; Ebisike, 2018).

Collectively, these spectral shifts provide definitive evidence of successful sol-gel encapsulation of rice-husk-ash-derived silica within the chitosan matrix. This structural integration is stabilized by robust hydrogen bonding and condensation reactions between the functional groups (hydroxyl and amine) of chitosan and the silanol groups of the silica phase (Ebisike, 2018). Ultimately, maintaining these active amine and hydroxyl binding sites alongside the newly introduced silica framework is anticipated to significantly enhance the composite's adsorption capacity compared to pure chitosan.

**Effect of Solution pH on Methylene Blue Adsorption**

The composite's removal performance was evaluated as a function of solution pH, which dictates the protonation state of the amine groups and the ionization of the silanol groups. Consequently, pH determines the net surface charge available to bind the cationic dye. Figure 9 illustrates the specific impact of solution pH on the removal efficiency of methylene blue.

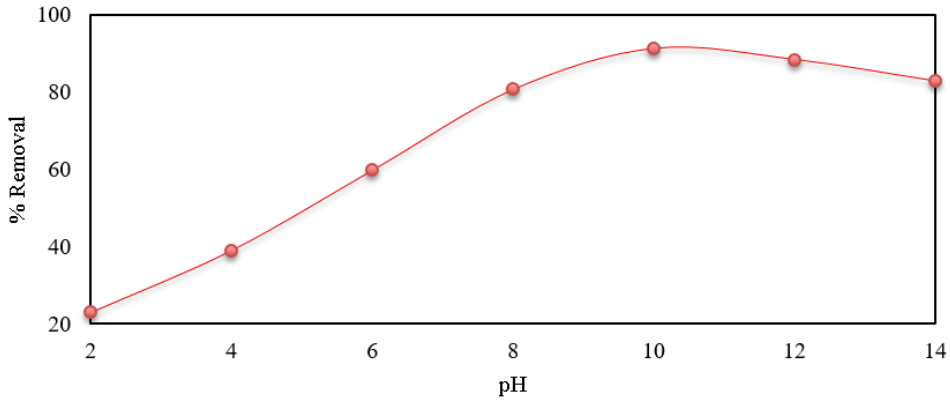



**Figure 9**: Effect of solution pH on the removal efficiency of methylene blue by the chitosan–silica composite.

Methylene blue (MB) removal peaked at 91.36% at pH 10, rising from 23.00% at pH 2, and subsequently falling to 82.92% at pH 14 (Figure 9). This trend depends directly on the surface charge of the composite. Below pH 7, protonated amine ($–NH_3^+$) and silanol ($–SiOH_2^+$), groups cause electrostatic repulsion with the cationic dye, while $H^+$ions compete for active sites. As pH increases toward pH 10, silanol groups deprotonate to siloxide

ions (Si–OH → Si–O⁻), generating a negative surface charge that strongly attracts the cationic MB. Past pH 10, efficiency drops slightly due to dye aggregation, hydroxylated dye species formation, $OH^-$ competition, and matrix destabilization (Kyzas & Bikiaris, 2015; Vakili *et al.*, 2019). These findings establish pH 10 as optimal, highlighting deprotonated silanol groups as the dominant binding sites (Blachnio *et al.*, 2023; Lan *et al.*, 2022; Zhong *et al.*, 2023).

**Effect of Adsorbent Dosage on Methylene Blue Adsorption**

The amount of adsorbent present dictates the number of active binding sites available for the dye in the solution. The accompanying graph in Figure 10 illustrates how varying the adsorbent dosage impacts the removal efficiency of methylene blue at an initial concentration of 50 mg/L.

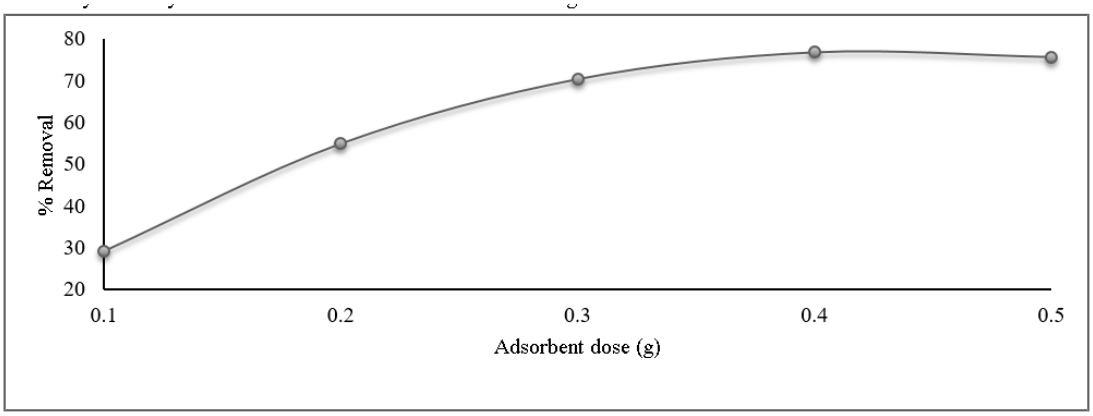



**Figure 10**: Effect of adsorbent dose on the removal efficiency of methylene blue.

As shown in Figure 10, the methylene blue (MB) removal efficiency rose sharply with the composite dosage, increasing from 29.06% at 0.1 g to a peak of 76.79% at 0.4 g, before marginally dropping to 75.66% at 0.5 g. The initial improvement is driven by a greater abundance of active functional groups, specifically the amine ($–NH_2$) and hydroxyl (–OH) groups from chitosan alongside the silanol (Si–OH) groups from the silica phase. Adsorption is primarily mediated by electrostatic attraction between MB and the negatively charged, deprotonated silanol surfaces, alongside hydrogen bonding and π–π interactions with the chitosan backbone. Conversely, the minor decline in efficiency beyond a 0.4 g dosage stems from particle aggregation and overlapping adsorption sites. This clumping reduces the effective surface area per unit mass and screens interior binding sites. Furthermore, under a fixed initial dye concentration, the excess adsorbent causes the available sites to approach saturation relative to the total dye molecules, reflecting typical mass-transfer and site-saturation limitations observed in chitosan-based composites.

**Effect of Contact Time on Methylene Blue Adsorption**

The equilibrium rate serves as a critical operational metric for adsorption processes. The Figure 11 illustrates how con-tact time influences the removal efficiency of methylene blue.

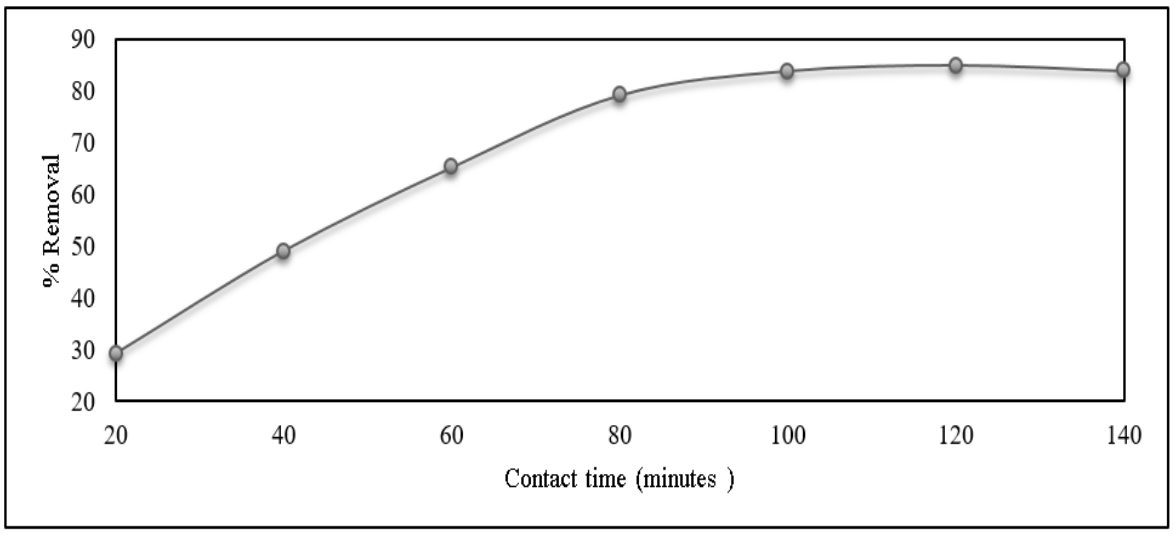



**Figure 11**: Effect of contact time on the removal efficiency of methylene blue.

Methylene blue (MB) removal efficiency rose sharply from 29.19% at 20 min to 79.19% at 80 min, before peaking at 84.92% after 120 min (Figure 11). This progression indicates that adsorption equilibrium occurred at the 120-minute mark, followed by a minor decline to 83.88% at 140 min. The rapid initial uptake is driven by the abundant active sites on the fresh composite surface and a steep concentration gradient that accelerates external mass transfer. Between 80 and 120 min, the adsorption rate slowed as external sites saturated, shifting the mechanism from surface binding to diffusion-controlled migration into the internal mesopores of the silica framework. The slight drop after 120 min suggests a shift toward desorption rather than net removal. At near-saturation, MB is held by weak, reversible electrostatic interactions and hydrogen bonding. Consequently, prolonged agitation can mechanically dissociate loosely bound molecules back into the solution as the concentration gradient diminishes.

**Effect of Initial Dye Concentration on Methylene Blue Adsorption**

To evaluate the influence of concentration on mass transfer and site availability, the initial methylene blue concentration was varied from 40 to 120 mg/L (Figure 12).

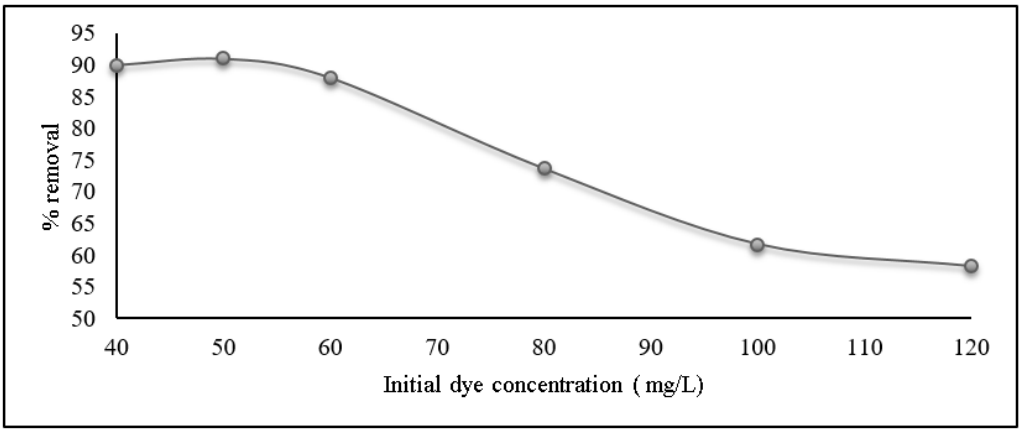



**Figure 12**: Effect of initial dye concentration on the removal efficiency of methylene blue by the chitosan–silica composite.

As shown in Figure 12, the removal efficiency of methylene blue (MB) remained relatively stable between 40 mg/L (90.00%) and 50 mg/L (91.00%). Beyond 50 mg/L, the removal percentage steadily declined, dropping to 88.00%, 73.64%, 61.69%, and 58.20% at initial concentrations of 60, 80, 100, and 120 mg/L, respectively. This trend aligns with the well-documented inverse relationship between initial dye concentration and percentage removal in fixed-dosage adsorption systems (Gebresslasie, 2020; Strebel *et al.*, 2024). At lower concentrations, the abundant amine, hydroxyl, and silanol functional groups easily accommodate the relatively few dye molecules. However, as the concentration increases, these active sites become saturated, leaving a larger fraction of the dye unadsorbed even though the total mass of dye bound per gram of adsorbent continues to increase (Gebresslasie, 2020; Strebel *et al.*, 2024). Consequently, 50 mg/L was selected as the optimal initial concentration for maximizing MB removal efficiency.

**Adsorption Isotherm Analysis**

The Langmuir and Freundlich isotherm models were applied to the equilibrium adsorption data to describe the interaction between methylene blue and the chitosan–silica composite surface at equilibrium, in line with common practice for chitosan–silica and other biopolymer composites (Blachnio *et al.*, 2023). Table 3 presents the isotherm parameters obtained.

Methylene blue (MB) adsorption onto the chitosan–silica composite was better described by the Langmuir model

**Table 3**: Langmuir and Freundlich isotherm parameters for the adsorption of methylene blue (MB) onto the chitosan–silica composite

| **Freundlich** | | | | **Langmuir** | | |
|---|---|---|---|---|---|---|
| Dye | 1/n | KF (mg/g) | $R^2$ | $K_L$ (L/mg) | $Q_m$ (mg/g) | $R^2$ |
| Methylene blue | 0.412 | 2.005 | 0.605 | 0.154 | 9.217 | 0.939 |

*1/n = heterogeneity factor; KF = Freundlich constant; $K_L$ = Langmuir constant; $Q_m$ = maximum adsorption capacity; $R^2$ = correlation coefficient.*

($R^2$ = 0.939) than the Freundlich model ($R^2$ = 0.605). This strong Langmuir fit indicates that the composite surface features relatively homogeneous binding sites rather than a highly heterogeneous distribution. This homogeneity aligns with the charge-selective binding mechanism of the dye, where MB selectively interacts with a single type of energetically uniform site specifically, the deprotonated silanol groups within the silica domain.

These findings mirror previous data for MB adsorption on pure chitosan, which also demonstrated a dominant monolayer adsorption process characterized by a Langmuir fit ($R^2$ = 0.9409) and a maximum adsorption capacity of 7.605 mg/g (Akhtar & Jamal, 2026). Within the Freundlich framework, the constant (KF = 2.005 mg/g) indicates a moderate adsorption capacity. The heterogeneity factor (1/n = 0.412), being below 1, signifies a heterogeneous adsorbent surface, favourable adsorption, and a capacity that escalates alongside dye concentration (Blachnio *et al.*, 2023). However, because the Freundlich model yielded a comparatively poor fit to the experimental data (R2 = 0.605), it was excluded from estimating the composite's adsorption capacity. The Langmuir model was utilized instead.

Based on the Langmuir isotherm, the maximum monolayer adsorption capacity ($Q_m$) of the composite for methylene blue was 9.217 mg/g, with a Langmuir constant ($K_L$) of 0.154 L/mg. The relatively high binding affinity is attributed to the small molecular size of methylene blue, which allows easy access to the interior binding sites, and to the strong electrostatic attraction between the negatively charged silanol groups of the silica domain and the cationic MB molecule at pH values above the point of zero charge of the composite (Liang, 2022). Overall, the good Langmuir fit indicates that methylene blue adsorption onto the chitosan–silica composite proceeds primarily as a monolayer on energetically similar, charge-complementary active sites until saturation is reached.

## CONCLUSION

This study successfully synthesized a chitosan–silica composite from two low-cost, waste-derived precursors. XRF showed silica as the dominant constituent of the composite (60.916% $SiO_2$), XRD showed the disappearance of the diagnostic (020) chitosan reflection at 2θ = 10.37° together with a broad amorphous hump, indicating that silica anchoring replaced chitosan's crystalline order with an amorphous silica network, while Raman spectroscopy revealed shifted and split vibrational bands consistent with a new hydrogen-bonded chitosan–silica network, and FT-IR confirmed Si–O–Si and Si–OH bands from successful sol-gel encapsulation. Batch adsorption studies identified optimal methylene blue removal at pH 10 (maximum removal of 91.36%), an adsorbent dose of 0.4 g, a contact time of 120 minutes, and an initial dye concentration of 50 mg/L, reflecting electrostatic attraction between the deprotonated silanol groups of the composite and the cationic dye, with the Langmuir isotherm ($R^2$ = 0.939) giving a maximum monolayer capacity ($Q_m$) of 9.217 mg/g. These findings demonstrate a sustainable, low-cost route for valorizing fisheries and agricultural waste into a potential adsorbent for methylene blue.

### Conflict of Interest

All the authors have declared that there is no conflict of financial or personal interest involved in the work described in this paper.

### Acknowledgements

The authors are grateful to the Department of Science Technology and Engineering, Kibabii University, for its support during this research.

## REFERENCES

Abdulrahman, F. I., Garba, Z. N., & Mohammed, I. U. (2021). Chitosan-based adsorbents for the removal of dyes from wastewater: a review. *Journal of Polymers and the Environment, 29*(6), 1723–1742.

Ade, M. R., Hidayat, N., & Sudarmadji, S. (2020). Preparation and characterization of chitosan from fish scales. *Journal of Applied Chemistry, 12*(3), 45–52.

Akhtar, M., & Jamal, A. (2026). Adsorption of methylene blue onto chitosan-based adsorbents: equilibrium and kinetic studies. *Journal of Environmental Chemical Engineering, 14*(2), 108–115.

Al Sagheer, F. A., & Muslim, S. (2009). Thermal and mechanical properties of chitosan-silica hybrid composites. *Carbohydrate Polymers, 77*(2), 305–311.

Bakar, N. A., Sapei, L., & Ismail, J. (2022). Extraction of silica from rice husk ash for composite synthesis. *Materials Chemistry and Physics, 278*, 125–134.

Blachnio, M., Zienkiewicz-Strzalka, M., Derylo-Marczewska, A., Nosach, L. V., & Voronin, E. F. (2023). Chitosan–silica composites for adsorption application in the treatment of water and wastewater from anionic dyes. *International Journal of Molecular Sciences, 24*(14), 11818.

Bratskaya, S., Pakhlov, E., & Privalko, V. (2022). Chitosan-silica hybrid materials: synthesis and characterization. *Journal of Sol-Gel Science and Technology, 102*(2), 235–246.

Brugnerotto, J., Lizardi, J., Goycoolea, F. M., Argüelles-Monal, W., Desbrières, J., & Rinaudo, M. (2001). An infrared investigation in relation with chitin and chitosan characterization. *Polymer, 42*(8), 3569–3580. https://doi.org/10.1016/S0032-3861(00)00713-8

Chun, S. H., & Lee, J. H. (2020). Calcination of rice husks for silica extraction. *Journal of the Korean Ceramic Society, 57*(4), 401–408.

Crini, G., & Badot, P. M. (2020). Application of chitosan, a natural amino polysaccharide, for dye removal from aqueous solutions by adsorption. *Progress in Polymer Science, 33*(4), 399–447.

Ebisike, K. (2018). FT-IR analysis of chitosan and chitosan-silica composites. *Journal of Chemical and Pharmaceutical Research, 10*(5), 112–118.

Elhady, M., Abdel-Aziz, H., & Abdel-Rahman, M. (2024). Recent advances in chitosan-based adsorbents for dye removal. *Journal of Water Process Engineering, 59*, 104–117.

Elzahar, M. M. H., Abdelhamid, H. N., & Guibal, E. (2023). Removal of direct dyes from aqueous solutions using chitosan-based materials. *Scientific Reports, 13*, 11426.

Ermania Em Wogo, A., Dee, M. Y., & Darmakusuma, D. (2022). The effect of silica concentration and chitosan on the antibacterial properties of silica immobilized

with EDTA-Cu and chitosan. 9th International Conference of the Indonesian Chemical Society (ICICS).

Gebresslasie, B. (2020). Effect of initial dye concentration on adsorption efficiency. *Journal of Environmental Management, 275*, 111–120.

Gisi, S. D., Lofrano, G., Grassi, M., & Notarnicola, M. (2020). Characteristics and adsorption capacities of low-cost sorbents for wastewater treatment: a review. *Sustainable Materials and Technologies, 23*, e00156.

Gupta, V. K. (2021). Application of chitosan-based materials for the removal of dyes from wastewater. *Environmental Technology & Innovation, 22*, 101–112.

Jonathan, O. (2020). Silica extraction from agricultural waste. *Waste Management, 105*, 102–110.

Kačuráková, M., Belton, P. S., & Wilson, R. H. (2020). Raman spectroscopy of chitosan. Spectrochimica Acta Part a: *Molecular and Biomolecular Spectroscopy, 74*(5), 1094–1099.

Kasaai, M. R. (2008). A review of several reported procedures to determine the degree of N-acetylation for chitin and chitosan. *Carbohydrate Polymers, 71*(4), 497–508.

Kaya, M., Baran, T., & Mentes, A. (2022). A review on fungal chitosan: extraction, characterization, and environmental applications. *Carbohydrate Polymers, 281*, 119056.

Khabibullaeva, E. S., Kuznetsov, B. N., & Kazachenko, A. S. (2022). Crystallographic structure of chitosan composites. *Journal of Structural Chemistry, 63*(4), 512–521.

Kyomuhimbo, H. D., McHunu, W., Arnold, M., Feleni, U., Haneklaus, N. H., & Brink, H. G. (2024). Synthesis and dye adsorption dynamics of chitosan–polyvinylpolypyrrolidone (PVPP) composite. *Polymers, 16*(18), 2555.

Kyzas, G. Z., & Bikiaris, D. N. (2015). Recent modifications of chitosan for adsorption applications: a critical and systematic review. *Marine Drugs, 13*(1), 312–337.

Lan, Y., Wang, S., & Zhao, X. (2022). Adsorption of methylene blue onto chitosan-silica composites. *Journal of Chemical Technology and Biotechnology, 97*(8), 2056–2065.

Li, J., Wang, X., & Zhao, G. (2024). Advances in sol–gel synthesis of chitosan–silica hybrids for wastewater treatment: a review. *Journal of Sol-Gel Science and Technology, 109*(2), 415–432.

Liang, T. (2022). Adsorption isotherm modeling for dye removal. *Chemical Engineering Research and Design, 180*, 234–245.

Maingi, F. M., Muya, E. M., & Kamau, G. N. (2022). Adsorption of chromium (VI) from aqueous solutions using chitosan composite. *South African Journal of Chemistry, 75*, 25–33.

Mishra, P. K., Singh, R., & Gupta, A. (2021). Low-cost adsorbents for wastewater treatment. *Environmental Chemistry Letters, 19*(2), 1245–1260.

Ngulube, T., Gumbo, J. R., & Dube, J. (2020). Adsorption of pollutants from aqueous solutions using low-cost adsorbents. *Environmental Science and Pollution Research, 27*(15), 17845–17862.

Rinaudo, M. (2020). Chitin and Chitosan: properties and applications. *Progress in Polymer Science, 31*(7), 603–632.

Rinaudo, M., Pavlov, G., & Desbrières, J. (1999). Influence of acetic acid concentration on the solubilization of chitosan. *Polymer, 40*(25), 7029–7032.https://doi.org/10.1016/S0032-3861(99)00056-7

Saiful, H. (2022). Synthesis and characterization of chitosan-silica composites. *International Journal of Chemistry, 12*(3), 78–89.

Sapei, L., Bakar, N. A., & Ismail, J. (2021). Sodium silicate extraction from rice husk ash. *Journal of Chemical Engineering, 28*(4), 312–320.

Soltani, R. D. C. (2021). Adsorption technologies for dye removal from industrial wastewater. *Journal of Environmental Chemical Engineering, 9*(5), 105234.

Strebel, S., Fuchs, H., & Keppler, K. (2024). Adsorption capacity of chitosan composites for cationic and anionic dyes. *Journal of Environmental Chemical Engineering, 12*(2), 112–124.

Stuart, B. (2004). Infrared spectroscopy: fundamentals and applications. John Wiley & Sons.

Vakili, M., Deng, S., Li, T., Wang, W., Wang, W., Yu, G., & Wang, X. (2019). Novel crosslinked chitosan for enhanced adsorption of contaminants from aqueous solutions: a review. *International Journal of Biological Macromolecules, 127*, 115–127. https://doi.org/10.1016/j.ijbiomac.2019.01.03

Wang, J., Wang, S., & Zhao, G. (2023). Advances in chitosan-based adsorbents for dye removal from aqueous systems. *Bioresource Technology Reports, 23*, 101123.

Xu, J., Zhang, Y., & Li, Q. (2021). Adsorption mechanisms of dyes on chitosan-based materials. *Journal of Molecular Liquids, 321*, 114456.

Younes, I., Rinaudo, M., & Jellouli, K. (2020). Extraction and characterization of chitin and chitosan from marine resources. *International Journal of Biological Macromolecules, 164*, 2294–2305.

Zhong, T., Xia, M., Yao, Z., & Han, C. (2023). Chitosan/silica nanocomposite preparation from shrimp shell and its adsorption performance for methylene blue. *Sustainability, 15*(1), 47. https://doi.org/10.3390/su15010047

Zhou, Y., Wang, H., & Zhang, X. (2022). Preparation and characterization of chitosan-silica composites. *Materials Research Bulletin, 148*, 111–122.